

www.acsami.org Research Article

Engineering Active Sites of Gold-Cuprous Oxide Catalysts for Electrocatalytic Oxygen Reduction Reaction

Aiai Zhang, Jinfang Wu,* Lei Xue, Caixia Li, Shanghong Zeng,* Dominic Caracciolo, Shan Wang, and Chuan-Jian Zhong*



Cite This: ACS Appl. Mater. Interfaces 2021, 13, 46577-46587



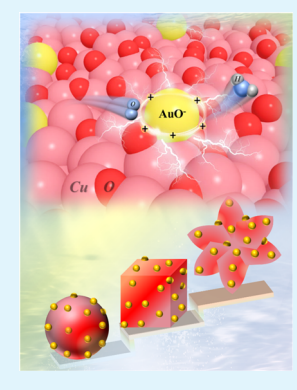
ACCESS

Metrics & More

Article Recommendations

s Supporting Information

ABSTRACT: Understanding how the catalyst morphology influences surface sites is crucial for designing active and stable catalysts and electrocatalysts. We here report a new approach to this understanding by decorating gold (Au) nanoparticles on the surface of cuprous oxides (Cu₂O) with three different shape morphologies (spheres, cubes, and petals). The Au-Cu₂O particles are dispersed onto carbon nanotube (CNT) matrix with high surface area, stability, and conductivity for oxygen reduction reaction. A clear morphology-dependent enhancement of the electrocatalytic activity is revealed. Oxygenated gold species (AuO⁻) are found to coexist with Au⁰ on the cube and petal catalysts, whereas only Au⁰ species are present on the sphere catalyst. The AuO⁻ species function effectively as active sites, resulting in the improved catalytic performance by changing the reaction mechanism. The enhanced catalytic performance of the petal-shaped catalyst in terms of onset potential, half-wave potential, diffusion-limited current density, and stability is closely associated with the presence of the most abundant AuO⁻ species on its surface. Highly active AuO⁻ species are identified on the surface of the catalysts as a result of the unique structural characteristics, which is



attributed to the structural origin of high activity and stability. This insight constitutes the basis for assessing the detailed correlation between the morphology and the electrocatalytic properties of the nanocomposite catalysts, which has implications for the design of surface-active sites on metal/metal oxide electrocatalysts.

KEYWORDS: gold-cuprous oxide, nanocomposite catalysts, morphology, oxygen reduction reaction, activated oxygen species

1. INTRODUCTION

Oxygen reduction reaction (ORR) is a key electrode process in electrochemical devices for clean and sustainable energy storage and conversion like metal-air batteries and fuel cells. $\overset{\Upsilon-3}{-}$ The high activation barrier leads to high overpotential and sluggish reaction kinetics for ORR, which strongly depends on active electrocatalysts to reduce the overpotential.⁴⁻⁶ Pt-based alloy electrocatalysts have been widely exploited as the most active electrocatalysts for ORR due to their synergistic catalytic properties.^{7,8} Nevertheless, Pt is scarce, which hinders their commercialization on a large scale. 9,10 Hence the development of other alloy catalysts ^{11,12} or Pt-free catalysts such as transition metals/metal oxides, ^{13–17} carbon-based materials, ^{18–20} chalcogenides, ²¹ spinels, ²² and metal-organic frameworks²³ has gained increasing interests. Among these materials, copper and copper oxide-based materials, especially cuprous oxide (Cu₂O), have been extensively studied in photocatalysis, solar cells, sensors, and electrocatalysis. 24-26 One intriguing example involves Cu@ Cu₂O core-shell nanocatalysts. The ORR polarization curves of such a catalyst exhibited an enhanced limit current density and onset potential ($E_{\text{onset}} = 0.93 \text{ V}$ vs reversible hydrogen electrode, RHE) via a four-electron transfer pathway.²⁷ Studies have also demonstrated that the Cu₂O nanoparticle catalysts showed enhancement in catalytic activity and durability for

ORR in comparison with commercial Pt/C in alkaline electrolytes. $^{28-30}$ Given the impressive catalytic performance of AuCu alloy catalysts $^{31-33}$ and the propensity of copper oxidation, the combination of $\rm Cu_2O$ and Au has also recently been explored for many technologically important applications, such as environmental cleanup, solar energy conversion, and gas sensing. $^{34-38}$ Although such catalysts have not been studied for ORR, studies of the catalysts in other catalytic or sensing systems have shown that Au-Cu₂O functions as photocatalyst for the removal of organic dyes and sensing materials for electrochemical detection for $\rm H_2O_2$. 39,40

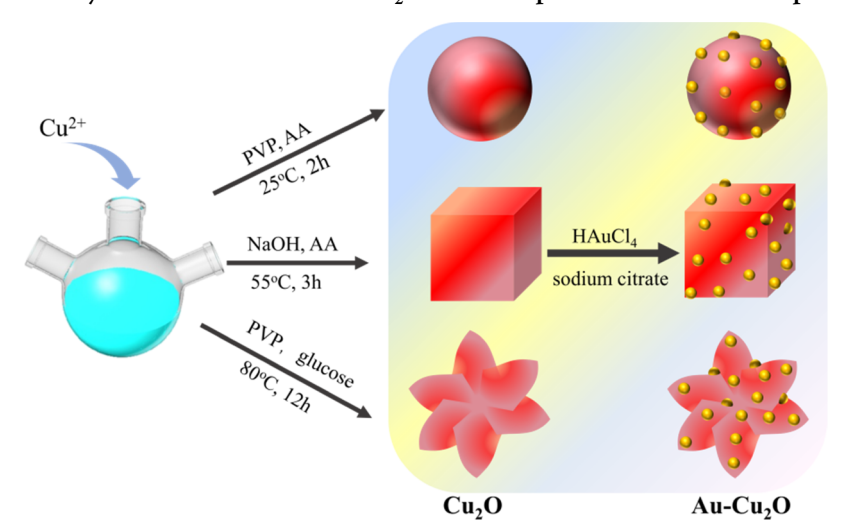
While the importance of the catalyst morphology in affecting the catalytic properties of the catalysts has been recognized, there has been little understanding of the mechanistic origin. For example, the shape-controlled synthesis is known for controlling the catalyst morphology, and the understanding of how it correlates with the catalytic activity and stability remains elusive. The shape and morphology of Cu₂O have been known

Received: June 23, 2021 Accepted: September 16, 2021 Published: September 27, 2021





Scheme 1. Illustration of the Synthetic Processes of Au-Cu₂O Nanocomposites with Three Morphologies



to play a vital role in ORR in alkaline media. Recent results from density functional theory (DFT) calculations reveal the adsorption and activation of O2 on the Cu2O(100) facet is stronger than that on the Cu₂O(111) facet. 41 Given the possibility of synthesizing Cu₂O particles with tunable lattice planes or/and controlled morphologies, there is an increasing interest to probe the origin of the morphology-dependent enhancement of catalytic activity.

Here, we demonstrate a new strategy for designing catalysts by decorating Au nanoparticles on the surface of Cu₂O with different shape morphologies (e.g., spheres, cubes, and petals) and dispersing them on a high-surface-area and conductive carbon nanotube (CNT) matrix (Au-Cu₂O/CNTs) as nanocomposite catalysts. In contrast to traditional use of carbon powders as support, we used CNTs as a catalyst dispersion metric, which is known to improve the conductivity and stability of the catalysts. 42 We investigated the relationship between the morphology and activity over the Au-Cu₂O/ CNTs nanocomposite catalysts of three different shapes, including spheres, cubes, and petals, aiming to reveal the origin of the enhanced catalytic activity. This design strategy allowed us to determine the surface sites, the interaction between Au and Cu2O, and their morphological effect on the activity. The findings on the morphology-activity relationship will deepen the understanding of nanocomposite catalysts for effective design of active and stable electrocatalysts for ORR.

2. EXPERIMENTAL SECTION

2.1. Synthesis of Cu₂O. The chemical reagents used in this work are described in the Supporting Information (SI). Cu₂O spheres were synthesized according to a previously reported method with a subtle modification. 43 Cu(Ac)₂·H₂O and poly(vinylpyrrolidone) (PVP) were mixed into ascorbic acid solution. The suspension was centrifuged and dried at 60 °C for 12 h to obtain the Cu₂O spheres.

The Cu₂O cubes were synthesized following a method. 44 Briefly, CuCl₂ solution was heated to 55 °C, and then NaOH and ascorbic acid were added to obtain a dark brown solution. The solution was kept at 60 °C for 12 h, followed by centrifugation and washing. Finally, the resulting Cu₂O cubes were precipitated.

For the preparation of petal-shaped Cu₂O, 1 mL of CuSO₄ solution was added dropwise into distilled water containing 0.216 g of PVP. Sequentially, 0.19 g of sodium citrate, 0.13 g of anhydrous sodium carbonate, and 0.25 g of glucose were gradually added into the solution, and then kept at 80 °C for 12 h, followed by centrifugation and washing. Finally, the resulting Cu₂O petal was precipitated.

2.2. Synthesis of Au-Cu₂O/CNTs. The Cu₂O particles were subsequently decorated with Au nanoparticles to form Au-Cu₂O particles. Au-Cu₂O particles were prepared by the one-pot approach (Scheme 1). Specifically, 98 mg of the above-prepared Cu₂O and 260 mg of sodium citrate were dispersed in 65 mL of distilled water. Then, 0.72 mL of HAuCl₄ (1 g/100 mL) was added into the above solution. The brownish black products were dried at 60 °C for 12 h under vacuum to obtain Cu₂O particles decorated with Au nanoparticles. In this process, citrate reduced AuCl₄⁻ to form small Au nanoparticles on the surface of Cu₂O.

The above Au-Cu₂O particles were then dispersed with high surface area and conductive CNT matrix and underwent a hydrothermal dispersion process to prepare the nanocomposite catalysts. Specifically, 0.49 g of CNTs and 98 mg of the impregnated Au-Cu₂O particles were dispersed in distilled water by sonication for 30 min. The solution was transferred into a Teflon-lined autoclave and made to react at 180 °C for 12 h. After the hydrothermal reaction, the precipitate was dried at 80 °C for 24 h and then calcined at 350 °C under N₂ for 3 h. Finally, the Au-Cu₂O/CNTs nanocomposite catalysts were obtained. Using this method, Au-Cu₂O sphere/CNTs, Au-Cu₂O cube/CNTs, and Au-Cu₂O petal/CNTs catalysts were prepared.

2.3. Catalyst Characterizations. The morphologies of the asprepared Au-Cu₂O catalysts were characterized by scanning electron microscopy (SEM, Hitachi S-4800), energy-dispersive X-ray (EDX), transmission electron microscopy (TEM, FEI Tecnai G2 F20 S-Twin), and high-resolution transmission electron microscopy (HRTEM). The structures of catalysts were obtained by power Xray diffraction (XRD) patterns on PANalytical X'pert PRO with Cu $K\alpha$ radiation at 100 mA and 40 kV. The surface properties of samples were analyzed by X-ray photoelectron spectroscopy (XPS) on Thermo ESCALAB 250XI with Al K α .

2.4. Catalytic Performance Measurement. A glassy carbon (GC) electrode (0.196 cm² with geometric area) was polished with $0.05 \mu m$ alumina powder and rinsed with distilled water and ethanol. The as-prepared nanocomposite (5 mg) was added into the solution containing 1 mL of isopropyl alcohol and 20 μ L of 0.5 wt % nafion and sonicated for 30 min to obtain a catalyst ink solution with uniform dispersion and no visible particles. Then, 10 μ L of the suspension was dropped on the surface of GC disk (loading content ~ 0.10 mg/cm^2).

Electrochemical measurements were performed in a three-electrode system using a microcomputer-controlled CH1760E electrochemical analyzer (CH Instruments). Hg/Hg2Cl2 (KCl, saturated), Pt plate and modified GC were used as the reference, counter, and working electrodes, respectively. The cyclic voltammetry (CV) and linear sweep voltammetry (LSV) measurements were carried out in 0.1 M KOH saturated with N2 and O2, respectively. The Koutecky-Levich

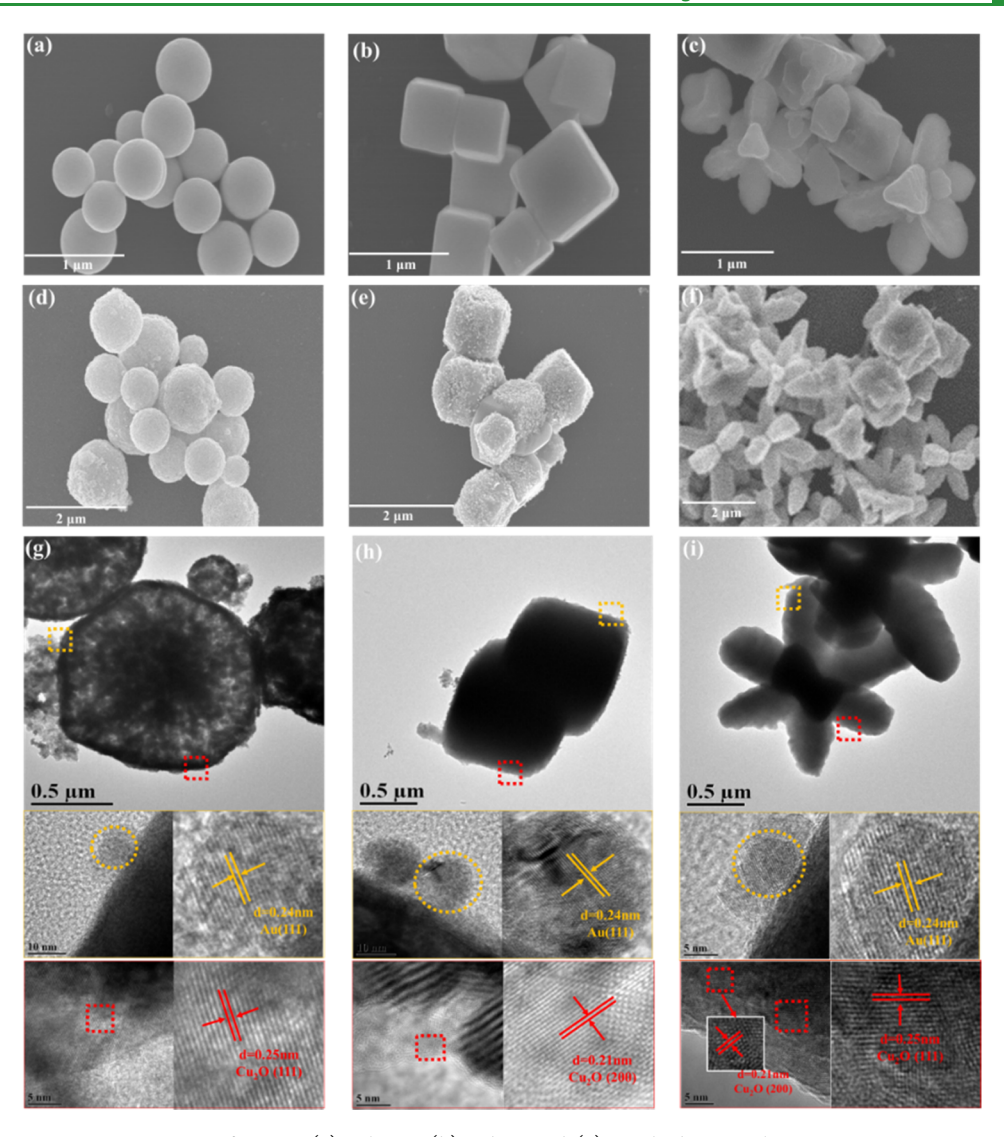


Figure 1. Top-row images: SEM images of Cu₂O: (a) spheres, (b) cubes, and (c) petals; bottom three-row images: SEM, TEM, and HRTEM images of Au-Cu₂O: (d, g) spheres, (e, h) cubes, and (f, i) petals.

(K-L) plots method was used to determine the number of electron transfers (n) under specific electrode potentials.

3. RESULTS AND DISCUSSION

3.1. Morphological and Structural Characteristics.

The morphology of Au-Cu₂O nanocomposite particles and distribution of Au nanoparticles on Cu₂O were examined using SEM, EDX elemental mapping, TEM, and HRTEM. Figure 1 (and Figure S1) shows three different distinctive morphologies, including spheres, cubes, and petals for the Au-Cu₂O nanocomposite catalysts synthesized in this work. In comparison with the relatively smooth surface features for Cu₂O (Figure 1a-c), the surface of the Au-Cu₂O nanocomposites (Figure 1d-f) exhibits relatively rough and uneven morphologies, characteristic of Au nanoparticles deposited on the surface of Cu₂O.

Detailed surface morphologies were analyzed by TEM and HRTEM (Figure 1g–i). The bright dots on Cu_2O spheres (~800 nm) in the TEM image (Figure 1g) are attributed to aggregated Cu_2O nanoparticles with oriented (111) facets. The HRTEM images revealed interplanar spacing distances of 0.24 and 0.25 nm, corresponding to Au(111) and $Cu_2O(111)$

facets. On the Au- Cu_2O cubes (an average edge length of 700 nm) (Figure 1h), mainly Cu_2O (200) and Au(111) crystal facets were detected, which shows lattice spaces of 0.21 and 0.24 nm, respectively. On the Au- Cu_2O petals (Figure 1i), the detected lattice fringes of Cu_2O indicate that Cu_2O petals expose, namely, two different lattice spaces of about 0.21 and 0.25 nm corresponding to (200) and (111) facets. It also detected the Au(111) lattice fringe of 0.24 nm for the Au(111) facet. To further understand the distribution of Cu and Cu species, the samples were also analyzed using Cu and Cu surface (Figure Cu).

CNTs were used as a matrix for dispersing the Au-Cu₂O nanocomposites, which also improve the conductivity and stability of catalysts due to their high specific surface area and excellent electrical conductivity. The Au-Cu₂O sphere, cube, and petal nanocomposites were shown to maintain original morphologies and display uniform dispersion on CNTs by the hydrothermal procedure (Figure S2). As in the Au-Cu₂O nanocomposites, the Cu₂O nanoparticles in Au-Cu₂O sphere/CNTs, Au-Cu₂O cube/CNTs, and Au-Cu₂O petal/CNTs still display (111), (200), and a mixture of (111) and (200) facets,

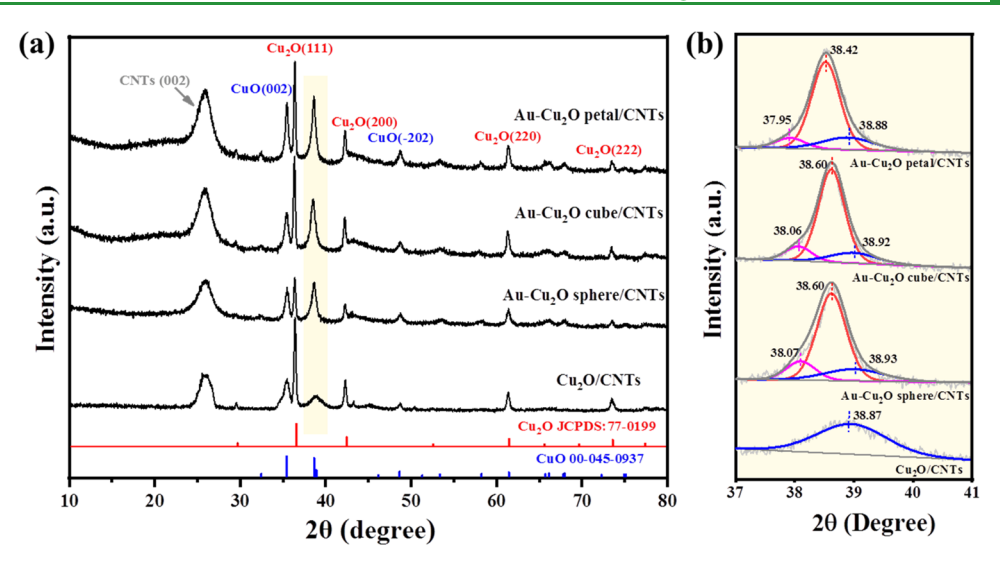


Figure 2. (a) XRD patterns of Au-Cu₂O sphere/CNTs, Au-Cu₂O cube/CNTs, Au-Cu₂O petal/CNTs, and Cu₂O/CNTs and (b) enlarged view of the peaks between 37 and 41°.

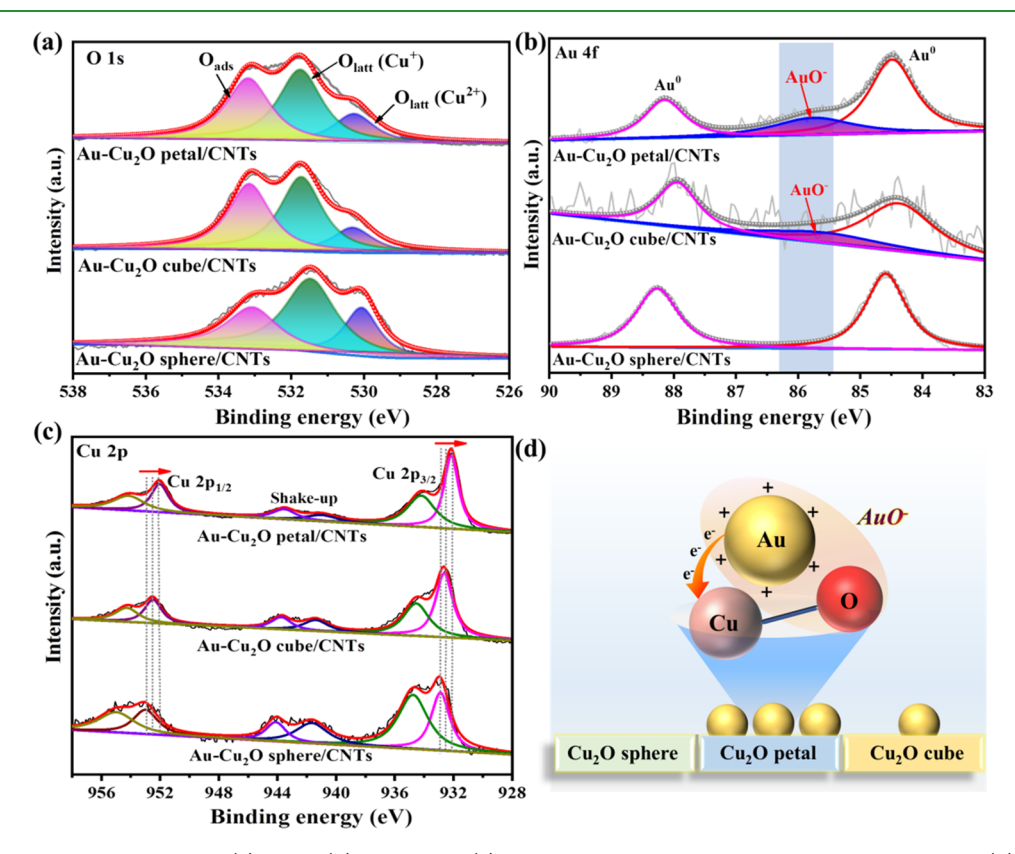


Figure 3. XPS spectra of the catalysts in (a) O 1s, (b) Au 4f, and (c) Cu 2p regions. Spectral deconvolution is included. (d) illustration of the surface AuO species on Cu2O sphere, cube, and petal.

respectively. XRD technique was used to confirm the structural features and crystalline phase of all of the catalysts. Figure 2a displays a typical set of XRD patterns for Au-Cu₂O sphere/ CNTs, Au-Cu₂O cube/CNTs, Au-Cu₂O petal/CNTs, and Cu₂O/CNTs. The diffraction peaks identified at 36.4, 42.2, 61.4, and 73.3° well match (111), (200), (220), and (222) facts of cubic Cu₂O (JCPDS 77-0199). The broad peak at 24.9° is originated from the (002) facet of CNTs. The diffraction peaks of CuO are observed at 32.5 and 48.7° (JCPDS 00-045-0937) after dispersing on CNTs (Figure S3). The hydrothermal dispersion process was shown to result in

the oxidation of part of the Cu₂O particles. As seen from the peaks between 37 and 41° in Figure 2b, the deconvolution reveals a peak at 38° corresponding to (111) facets of Au (JCPDS 04-0784), which is consistent with the XRD pattern of Au-Cu₂O nanocomposites (Figure S3). In contrast to Au-Cu₂O, the peak at ~38.5° of Au-Cu₂O/CNTs is identified to be originated from the AuCu alloy structure in Au-Cu₂O/ CNTs, suggesting that the hydrothermal dispersion process of Au-Cu₂O particles on CNTs also induces a certain degree of reduction of part of Cu₂O followed by alloying with Au.

Table 1. Results of the Relative Surface Composition Ratios from XPS Analysis of the Au-Cu₂O/CNTs Catalysts

	ratio (%)						
catalysts	$O_{latt} (Cu^{2+})/O$	$O_{latt} (Cu^+)/O$	O _{ads} /O	AuO ⁻ /Au			
Au-Cu ₂ O sphere/CNTs	13.2	45.5	41.3	0			
Au-Cu ₂ O cube/CNTs	13.5	45.4	41.1	18.9			
Au-Cu ₂ O petal/CNTs	19.4	47.9	32.7	23.1			

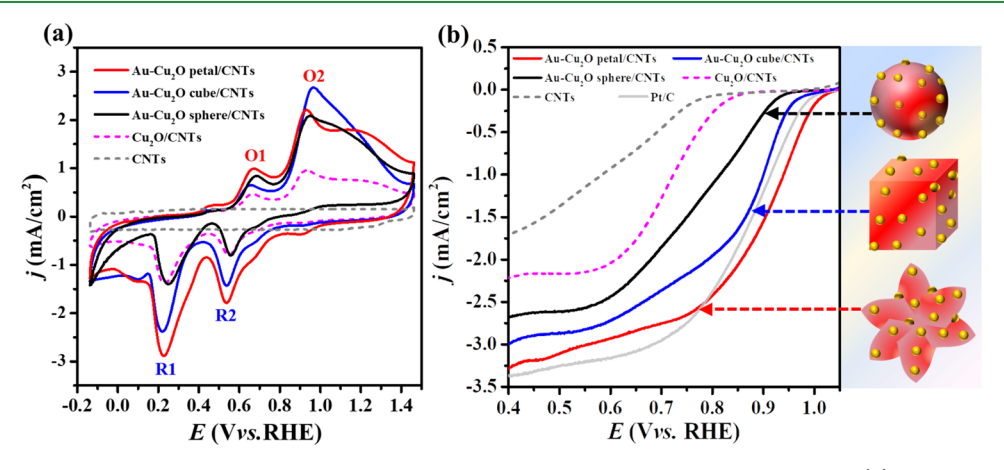


Figure 4. (a) CV curves of the catalysts at a scan rate of 50 mV/s in 0.1 M KOH solution saturated with N_2 and (b) LSV at a scan rate of 10 mV/s and rotation speed of 1600 rpm in 0.1 M KOH solution saturated with O_2 .

Table 2. Comparison of the Results from Studies of the Electrocatalytic ORR in Alkaline Solutions between This Work and Other Works

catalysts	onset potential	n	$E_{1/2}$ (V vs RHE)	Tafel slope (mV/dec)	mass activity (mA/mg $_{Au-Cu_2O}$) at 0.80 V	refs
Au-Cu ₂ O sphere/CNTs	0.92	4.00	0.83	79.6	90.2	this work
Au-Cu ₂ O cube/CNTs	0.95	3.99	0.88	70.6	92.8	this work
Au-Cu ₂ O petal/CNTs	0.99	3.98	0.91	68.7	138.5	this work
Cu@Cu ₂ O	0.93	3.97	0.86			27
Cu ₂ O nanocrystals	0.72	3.70	0.57			28
AuNi-Cu ₂ O	0.91	4.00	0.82	64.8		30
Cu ₂ O truncated octahedral	0.80	3.74	0.65			41
Cu_2O	0.79	1.80	0.73			56
Co_3O_4 - $CuO/Cu_2O/C$	0.86	4.00	0.72	83.6		57
Cu _x O ⁻ C/PANI	0.90	3.89	0.76			58

3.2. Surface and Lattice Oxygen Species. XPS analysis was used to investigate the oxidation states and partial charges on the Au-Cu₂O sphere/CNTs, Au-Cu₂O cube/CNTs, and Au-Cu₂O petal/CNTs catalysts (Figures 3 and S4). The O 1s spectra (Figure 3a) can be deconvoluted into three peaks. Based on the literature data, ^{39,47} the peaks at 530.2, 531.4, and 533 eV can be attributed to the lattice oxygen of CuO (O_{latt} (Cu²⁺)), lattice oxygen of Cu₂O (O_{latt} (Cu⁺)), and adsorbed oxygen (O_{ads}), respectively. The O_{ads} peak originates chemisorbed and dissociated oxygen species including O₂⁻, O²⁻, or O⁻, and hydroxide ion (OH⁻), which could be used to estimate the oxygen adsorption ability. ⁴⁸

As shown in Table 1, the relative ratio of O_{ads} vs the total detected O species is found to follow the order of Au-Cu₂O sphere/CNTs > Au-Cu₂O cube/CNTs > Au-Cu₂O petal/CNTs. This indicates that the Au-Cu₂O petal/CNTs exhibits a relatively weaker oxygen adsorption ability. In other words, Au-Cu₂O petal/CNTs contains a relatively larger amount of lattice oxygen, implying a stronger interaction between Au and Cu₂O in Au-Cu₂O particles by electronic effects. This assessment is demonstrated by the analysis of Au 4f and Cu 2p peaks. For Au 4f spectra in Figure 3b, the two peaks at 84.5 and 88.2 eV

suggest the existence of metallic Au particles in all of the three catalysts. For Au-Cu₂O cube/CNTs and Au-Cu₂O petal/CNTs catalysts, the deconvoluted peak at 85.7 eV is identified as Au⁺ species, which can be effectively stabilized as AuO species by the metal oxide support and the charge transfer process, suggesting a strong Au-O bond from Au and lattice oxygen in Cu₂O.⁴⁹⁻⁵¹ Herein, the presence of AuO species involves the charge transfer and rearrangement at the interface between Au atom and Cu₂O. As shown in Figure 3d and Table 1, Au-Cu₂O petal/CNTs catalyst has the most AuO species compared with Au-Cu₂O sphere/CNTs and Au-Cu₂O cube/CNTs, featuring the most lattice oxygen species.

Based on the microscopic morphologies of Cu₂O, Cu₂O petals are shown to expose mixed facets of (111) and (200) and form AuO⁻ species. AuO⁻ species is usually linked to the active species, which facilitates the insertion of oxygen atoms during the redox reaction. ^{40,52,53} Given this finding, the AuO⁻ species is believed to be active sites for ORR. The ORR activity is closely linked to the AuO⁻ species in addition to external O_{ads} species, which is substituted in the next section. As shown by Cu 2p spectra in Figure 3c, the peaks at 932.5 and 952.4 eV correspond to Cu 2p_{3/2} and Cu 2p_{1/2}, respectively; the satellite

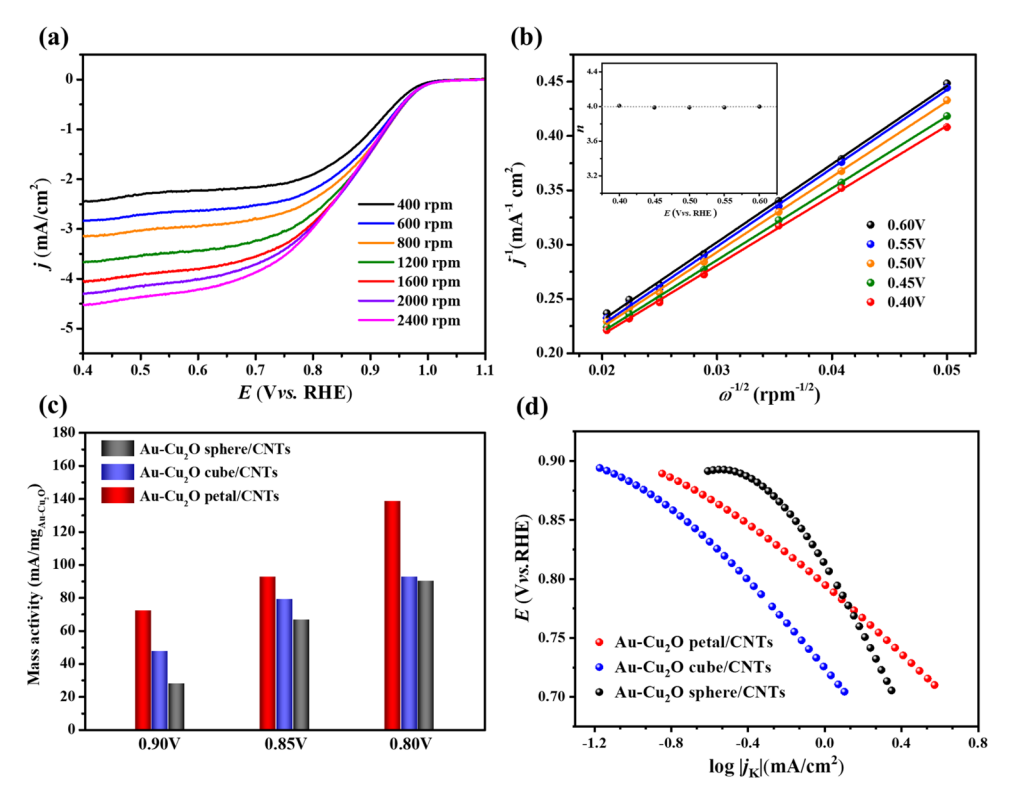


Figure 5. (a) RDE-LSV polarization curves in O_2 -saturated 0.1 M KOH solution with different rotation speeds at a scan rate of 10 mV/s; (b) corresponding K-L plots at different electrode potentials of the Au-Cu₂O petal/CNTs catalyst (inset: the transferred electron number versus potentials); (c) mass activity of all of the catalysts at 0.80, 0.85, and 0.90 V, and (d) Tafel plots of catalysts.

peaks appear at about 943.2 eV.⁵⁴ This result is indicative of the presence of CuO in the three catalysts. Interestingly, the peaks of Au-Cu₂O petal/CNTs show a subtle shift toward lower binding energy in comparison with those of Au-Cu₂O sphere/CNTs and Au-Cu₂O cube/CNTs. This shift indicates a stronger interaction between Au nanoparticles and Cu₂O petal, which improves the ORR catalytic activity. Furthermore, the subtle shift of the Cu 2p peaks of Au-Cu₂O petal/CNTs to a lower binding energy also demonstrates a stronger interaction between Au and Cu₂O species than those of the other two catalysts.

3.3. Electrocatalytic Properties. The electrocatalytic properties of the catalysts were assessed by cyclic voltammetry (CV) and liner sweep voltammetry (LSV) using the rotating disc electrode (RDE). The data were recorded after 50 cycles to gain stable performance of the catalysts. Figure 4 displays CV and LSV curves in 0.1 M KOH solution saturated with N₂ and O2, respectively. There are two pairs of redox peaks for the Au-Cu₂O/CNTs and Cu₂O/CNTs catalysts (Figure 4a). O1 and R1 represent the formation and reduction of Cu-OH_{ads}. O2 stands for further oxidation of Cu₂O to Cu²⁺, which can be represented by $Cu_2O + H_2O \rightarrow 2Cu^{2+} + 2e^- + 2OH^-$, whereas R2 corresponds to the reduction of Cu²⁺ species to Cu^{+,55} In contrast, the CV curve of CNTs displays only the featureless double-layer charging current, which is similar to those for typical CNTs. Furthermore, the electrocatalytic activity was analyzed at a rotation rate of 1600 rpm and the half-wave potentials were evaluated, as shown in Figure 4b and Table 2. Clearly, LSV curves demonstrate that the ORR catalytic activity strongly depends on the morphology of the catalysts. As seen from Figure S5, the introduction of CNTs as a matrix for dispersing the Au-Cu₂O nanocomposites is an effective way to improve the catalytic activity for ORR. The Au-Cu₂O petal/

CNTs nanocomposite catalyst exhibits superior performance among the three catalysts. In comparison with the exposed (111) facet Au-Cu₂O sphere/CNTs and (200) facet for Au-Cu₂O cube/CNTs, the Au-Cu₂O petal/CNTs catalyst is dominated by exposure of (111) and (200) facets. This catalyst shows the highest onset potential, half-wave potential ($E_{1/2}$), and diffusion-limited current density. The half-wave potential is in the order of Au-Cu₂O petal/CNTs (0.91 V) > commercial Pt/C (0.90 V) > Au-Cu₂O cube/CNTs (0.88 V) > Au-Cu₂O sphere/CNTs (0.83 V) > Cu₂O/CNTs (0.76 V) > CNTs (0.64 V) (see Table 2). Considering the fact that this catalyst is also mostly enriched with AuO⁻, AuO⁻ species has more positive influence on the electrocatalytic performance toward ORR.

To further elucidate the catalytic mechanism and kinetics, a series of LSV curves were obtained at different rotation speeds shown in Figures 5a and S6. At the same time, the corresponding Koutecky-Levich (K-L) plots at various potentials were also analyzed as shown in Figure 5b. The diffusion current density was shown to gradually increase with the rotation speed from 400 to 2400 rpm. The corresponding K-L plots exhibit a good linearity in the range from 0.4 to 0.6 V, displaying a first-order reaction characteristic. The average number of exchanged electrons (n) was extracted from the slope of K–L plot. The value of *n* for ORR on Au-Cu₂O petal/ CNTs, Au-Cu₂O cube/CNTs, and Au-Cu₂O sphere/CNTs is about 4, whereas the value of n for $Cu_2O/CNTs$ is 2.84, demonstrating that ORR on Au-Cu₂O/CNTs involves a fourelectron pathway. The magnitude of kinetic current density (j_K) at various potentials is in the order of Au-Cu₂O petal/ CNTs > Au-Cu₂O cube/CNTs > Au-Cu₂O sphere/CNTs (Figure S7), indicating that Au-Cu₂O petal/CNTs shows the highest enhancement in the kinetic rate.

Figure 5c shows the mass activity at 0.75, 0.80, 0.85, and 0.90 V. The mass activities were given in terms of the kinetic current per unit weight of Au-Cu₂O rather than the Au only content considering the substantial contribution of the catalytic activity of Cu₂O species. It is important to note that the catalysts were prepared by the same procedure in terms of loading Au nanoparticles on Cu₂O with different shapes. As shown in Table S1, by comparing Au loading of Au-Cu₂O sphere/CNTs vs the synthetic feeding ratio, the close agreement between the Au loading and the feeding value indicates that the content of Au in Au-Cu₂O/CNTs catalysts can be controlled well by controlling the feeding ratio of the Au precursors in the catalyst preparation. The mass activity of Au-Cu₂O petal/CNTs is the greatest, as evidenced by the mass activity at 0.80 V (V vs RHE) in the order of Au-Cu₂O petal/ CNTs (138.5 mA/mg_{Au-Cu₂O}) > Au-Cu₂O cube/CNTs (92.8 mA/mg_{Au-Cu₂O}) > Au-Cu₂O sphere/CNTs (90.2 mA/ mg_{Au-Cu,O}) (Table 2). Furthermore, as shown by the Tafel plots, the Tafel slopes for Au-Cu₂O petal/CNTs, Au-Cu₂O cube/CNTs, and Au-Cu₂O sphere/CNTs are 68.7, 70.6, and 79.6 mV/dec, respectively. All of the values are lower than that for a commercial Pt/C (80.4 mV/dec) (see Figure 5d and Table 2).³⁰ To further evaluate the electron transfer properties of the catalysts, Nyquist plots were obtained from electrochemical impedance spectroscopy (EIS) analysis. As shown in Figure S8, the charge transfer resistances of Au-Cu₂O/CNTs catalysts are all lower than that of Au-Cu₂O, indicating that CNTs contribute to improve the electrochemical conductivity. In comparison with the results from others as shown in Table 2, the Au-Cu₂O/CNTs catalyst with a petal shape is clearly shown to exhibit a superior catalytic performance at a similar level with the catalyst. $^{27,28,30,41,56-58}$

3.4. Catalyst Durability. The determination of long-term durability is a vital factor for evaluating the performance of catalysts. The durability of the catalysts was evaluated by chronoamperometric measurements (i-t) over a period of 10 h under a constant potential of 0.7 V vs RHE (working voltage of the fuel cell) at a rotation rate of 1600 in O₂-saturated 0.1 M KOH solution. As shown in Figure 6, the Au-Cu₂O petal/

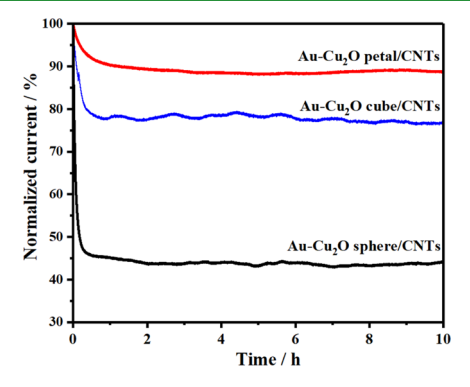


Figure 6. Chronoamperometric curves for the catalysts at $0.7~{\rm V}$ in ${\rm O}_2$ -saturated $0.1~{\rm M}$ KOH solution.

CNTs nanocomposite retains 89% of its original current density or shows a decrease by 11%, after about 10 h, while the Au-Cu₂O cube/CNTs and Au-Cu₂O sphere/CNTs retain only about 74 and 43% of their original current densities, respectively. Moreover, Au-Cu₂O petal only retains about 32% of the original current densities, while Au-Cu₂O petal/

CNTs can maintain 89% of its original current density, clearly confirming that CNTs as a catalyst dispersion matrix can improve the stability of the catalysts. The improved ORR stability of the Au-Cu₂O catalyst with the petal morphology may be attributed to its polycrystal structure (a mixture of Cu₂O(111) and (200) facets), which is in contrast to the cube and sphere morphologies where single-crystal Cu₂O (200) and (111) facets are detected, respectively. Mechanistically, the higher stability of Au-Cu₂O petal/CNTs could be explained on the basis of a weaker interaction of oxygen with the mixed surface facets of Cu₂O, resulting in a higher resistance toward self-oxidation to CuO during ORR. Overall, it is clear that the Au-Cu₂O petal/CNTs nanocomposite exhibits not only superior electrocatalytic performance but also remarkable electrochemical stability.

To understand the origin of the superior stability and stability of Au-Cu₂O petal/CNTs in comparison with the other catalysts, we systematically investigated the morphology, structure, and composition of Au-Cu₂O petal/CNTs and Au-Cu₂O cube/CNTs after the 10 h test. Figure 7a shows that the Au-Cu₂O petal/CNTs largely maintain the original morphology, while the surface layer was oxidized to CuO(110) compared with the fresh Au-Cu₂O petal/CNTs catalyst. This indicates Au-Cu₂O petal/CNTs is stable under ORR conditions. In contrast, the morphology of Au-Cu₂O cube/ CNTs was changed, as shown in Figure 7b, in comparison with the fresh catalyst. Importantly, the change of the morphology led to the exposure of CuO(002) and Cu₂O(111), indicating that Au-Cu₂O cube/CNTs is unstable and easily oxidized to CuO under ORR conditions. As shown in Figure S10, by analyzing the data, the Au-Cu₂O sphere/CNTs nanocomposite catalyst is apparently unstable due to the propensity of oxidation. Both activity and stability strongly depend on the morphology of the catalysts.

To substantiate the above findings, XRD and XPS were used to probe the structural changes of the Au-Cu₂O petal/CNTs and Au-Cu₂O cube/CNTs after the 10 h test. As shown from XRD in Figure 7c, Au-Cu₂O petal/CNTs catalyst's diffraction peaks are characteristic of Cu₂O and CuO, whereas the Au-Cu₂O cube/CNTs catalyst's diffraction pattern largely matches that of CuO. This finding is consistent with the results of TEM analysis. In comparison with the XPS spectra of fresh Au-Cu₂O petal/CNTs and Au-Cu₂O cube/CNTs (Figure 3), the Cu 2p peaks for the nanocomposite catalysts are shown to undergo subtle changes in which the peaks of Cu²⁺ are increased due to the appearance of oxidation, especially for Au-Cu₂O cube/ CNTs (Figure 7d). In view of this change, the Cu₂O species in the catalysts is likely oxidized to form Cu²⁺ in which the electrons are transferred to the ORR. The degree of oxidation can be reduced to a certain extent by designing Au-Cu₂O nanocomposite catalysts with stable morphology and structure. These findings clearly indicate that the Au-Cu₂O petal/CNTs catalyst is both active and stable in the alkaline environment, promising for use in alkaline fuel cells.

3.5. Mechanistic Considerations. We further performed density functional theory (DFT) calculations to understand mechanistic details involved in the adsorption of O_2 molecules on the Au-Cu₂O surface and the role of $Cu_2O(111)$ slab as the predominant facet in the enhanced activity mechanism. Au clusters with seven atoms supported on the $Cu_2O(111)$ surface were used as a model of the $Au-Cu_2O$ system in interaction with the O_2 molecule (see SI). There are three stable adsorption configurations as shown in Figure 8a. It is found

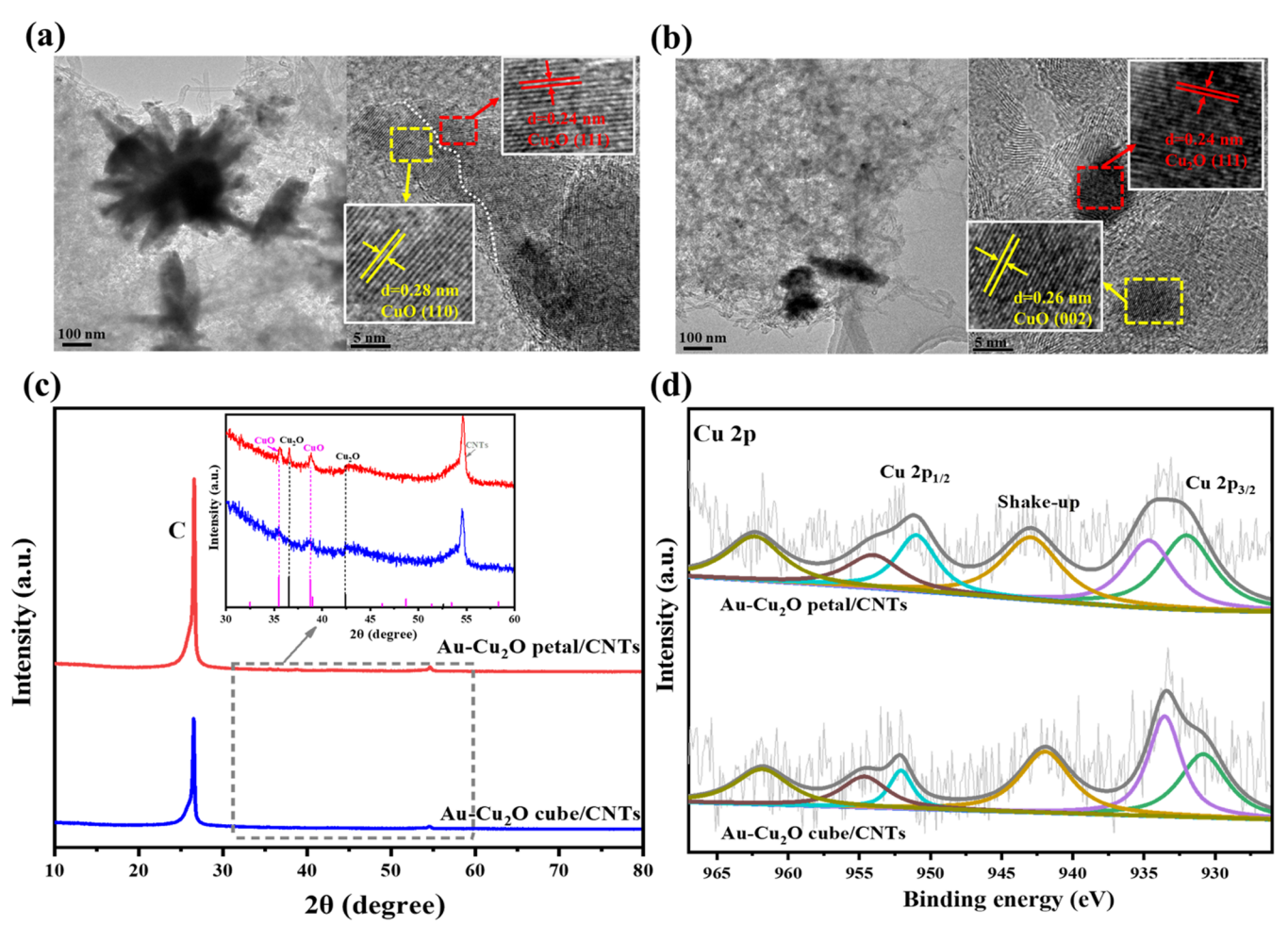


Figure 7. Morphology and structure of the catalysts after 10 h test. TEM and HRTEM images of (a) Au-Cu₂O petal/CNTs and (b) Au-Cu₂O cube/CNTs, and the corresponding (c) XRD patterns and (d) XPS spectra in the Cu 2p region.

that the most probable adsorption mode of O2 adsorbed on Au-Cu₂O is the bridge mode between Cu and Au atoms with an optimal compromise adsorption energy of -0.235 eV. The lengths of O-Cu, O-Au, and O-O are 2.286, 2.398, and 1.334 Å, respectively. Predictably, the optimal compromise of the adsorption or bond lengths is beneficial to activate and accelerate the kinetics of O-O bond splitting. It has been proven that molecular oxygen mainly prefers to adsorb on the pure Cu₂O surface by bridge mode. 41,59 Thus, the addition of Au clusters could regulate the adsorption configuration of the O2 molecule and then influence the ORR.

Taken together, the improved ORR activity for Au-Cu₂O/ CNTs catalysts is believed to originate from the change of the catalytic mechanism compared with Cu2O/CNTs, as illustrated in Figure 8b. ORR over the Cu₂O/CNTs catalyst may proceed through the two-electron pathway. Namely, the O2 molecule adsorbs on Cu atoms by bridge sites and is activated to form HOO* intermediate, and finally H2O2 is produced by a two-electron transfer reaction. However, Au nanoparticlemodified Cu₂O nanocomposites provide a four-electron pathway. Briefly, the addition of Au atoms generates an electronic effect between Au nanoparticles and Cu₂O on the formation of AuO species as efficiently active sites. AuO species accelerate the kinetics of O-O bond splitting, further facilitating the direct reduction of O2 to OH though a fourelectron process. Consequently, the faster dissociation rate of O-O bonds on the interface of Au and Cu₂O enhances the

ORR. As shown earlier, Au-Cu₂O/CNTs with the petal morphology possesses a maximum amount of AuO species, which exhibits the superior activity and stability for ORR. This mechanistic finding presents an intriguing pathway for understanding of the design parameters not only for copperbased alloy catalysts but also for other metal/metal oxide catalysts.

4. CONCLUSIONS

In conclusion, we have designed and synthesized new Au-Cu₂O/CNTs nanocomposite catalysts with three different controllable structures and morphologies. The Au-Cu₂O petal/ CNTs catalyst is shown to feature (111) and (200) facets of Cu₂O on the surface, whereas the Au-Cu₂O cube/CNTs and Au-Cu₂O sphere/CNTs catalysts display the (200) and (111) facets, respectively. AuO - species are shown to form as a result of the charge transfer and rearrangement between Au and lattice oxygen in the Cu₂O. The AuO⁻ species function as active sites in the improved catalytic performance for ORR by converting the two-electron pathway over the Cu₂O/CNTs catalyst to the four-electron pathway over Au-Cu₂O/CNTs catalyst. The Au-Cu₂O petal/CNTs exhibits a maximum ORR activity and stability with a half-wave potential of 0.91 V, outperforming the Au-Cu₂O cube/CNTs and Au-Cu₂O sphere/CNTs catalysts. The Au-Cu₂O petal/CNTs catalyst also shows superior stability due to its stability of morphology

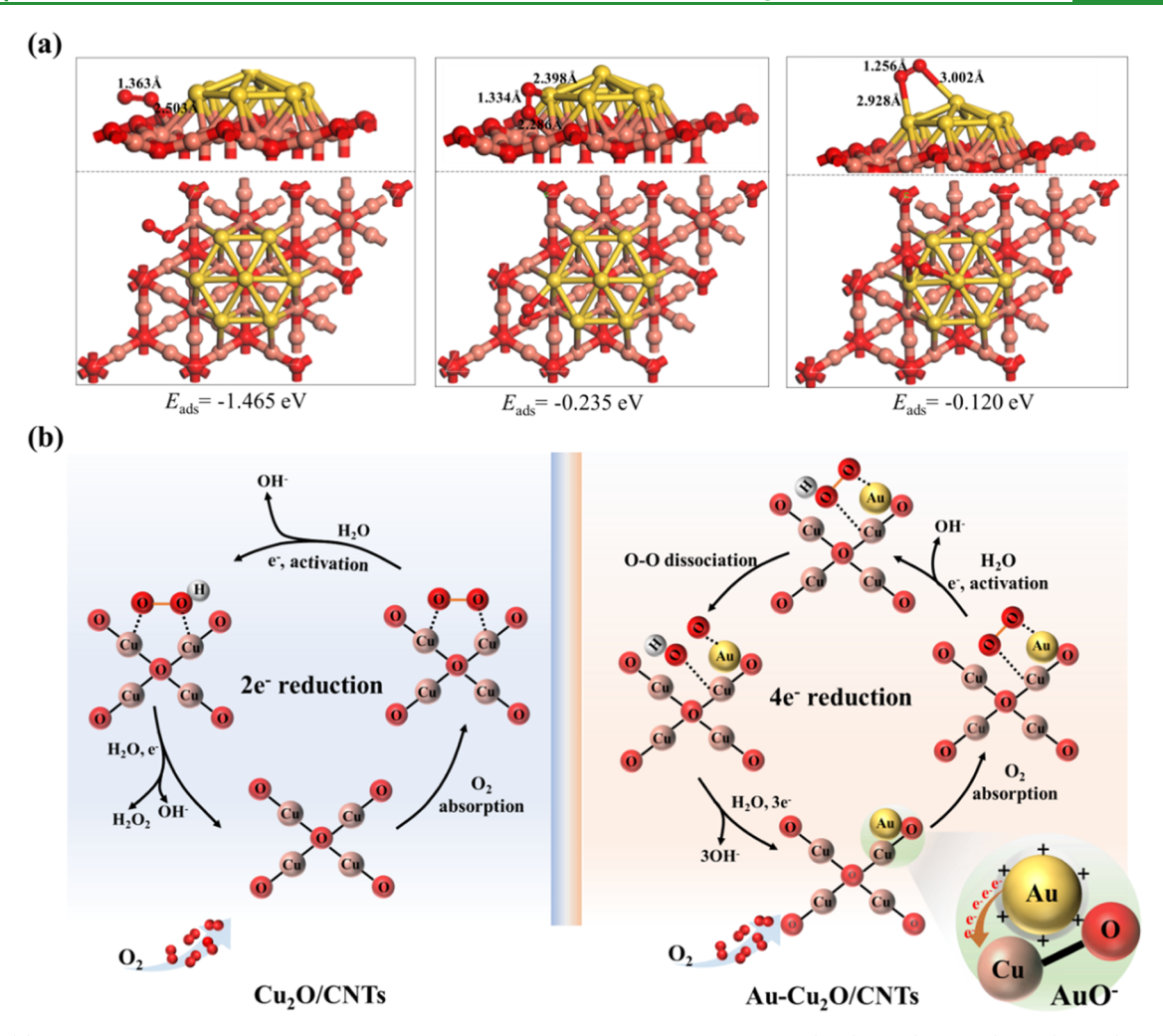


Figure 8. (a) Top and side views of three optimized configurations of O_2 adsorption on Au-Cu₂O(111); Cu (light red), Au (yellow), and O (red). (b) Schematic illustrations of the proposed ORR mechanisms on Cu₂O/CNTs and Au-Cu₂O/CNTs catalysts.

and structure under ORR conditions. These findings demonstrate that the nanocomposite catalysts can be manipulated by controlling the surface sites and catalytic mechanism of the catalysts, which provides a fresh insight into the rational morphological design of active and stable metal/metal oxide catalysts and electrocatalysts.

ASSOCIATED CONTENT

Supporting Information

The Supporting Information is available free of charge at https://pubs.acs.org/doi/10.1021/acsami.1c11730.

Experimental and computational details; EDX mapping and XRD of Au-Cu₂O; SEM, TEM, and XPS of Au-Cu₂O/CNTs; LSV curves and the corresponding K–L plots of Au-Cu₂O/CNTs; kinetic current density of Au-Cu₂O/CNTs; Nyquist plot of Au-Cu₂O/CNTs; and chronoamperometric curves of Au-Cu₂O (PDF)

AUTHOR INFORMATION

Corresponding Authors

Jinfang Wu — College of Chemistry and Chemical Engineering, Inner Mongolia Engineering and Technology Research Center for Catalytic Conversion and Utilization of Carbon Resource Molecules, Inner Mongolia University, Hohhot 010021, P. R. China; orcid.org/0000-0003-2615-9995; Email: jfwu@imu.edu.cn

Shanghong Zeng — College of Chemistry and Chemical Engineering, Inner Mongolia Engineering and Technology Research Center for Catalytic Conversion and Utilization of Carbon Resource Molecules, Inner Mongolia University, Hohhot 010021, P. R. China; orcid.org/0000-0002-6770-6214; Email: zengshanghong@imu.edu.cn

Chuan-Jian Zhong — Department of Chemistry, State University of New York at Binghamton, Binghamton, New York 13902, United States; orcid.org/0000-0003-0746-250X; Email: cjzhong@binghamton.edu

Authors

Aiai Zhang — College of Chemistry and Chemical Engineering, Inner Mongolia Engineering and Technology Research Center for Catalytic Conversion and Utilization of Carbon Resource Molecules, Inner Mongolia University, Hohhot 010021, P. R. China

Lei Xue — College of Chemistry and Chemical Engineering, Inner Mongolia Engineering and Technology Research Center for Catalytic Conversion and Utilization of Carbon Resource Molecules, Inner Mongolia University, Hohhot 010021, P. R. China

Caixia Li — College of Chemistry and Chemical Engineering, Inner Mongolia Engineering and Technology Research Center

- for Catalytic Conversion and Utilization of Carbon Resource Molecules, Inner Mongolia University, Hohhot 010021, P. R. China
- Dominic Caracciolo Department of Chemistry, State University of New York at Binghamton, Binghamton, New York 13902, United States
- Shan Wang Department of Chemistry, State University of New York at Binghamton, Binghamton, New York 13902, United States

Complete contact information is available at: https://pubs.acs.org/10.1021/acsami.1c11730

Notes

The authors declare no competing financial interest.

ACKNOWLEDGMENTS

The authors acknowledge support of the National Natural Science Foundation of China (grant nos. 22068026 and 21968020). C.J.Z. acknowledges the support of the National Science Foundation (CHE 2102482).

REFERENCES

- (1) Nguyen, D. C.; Doan, T. L. L.; Prabhakaran, S.; Tran, D. T.; Kim, D. H.; Lee, J. H.; Kim, N. H. Hierarchical Co and Nb Dualdoped MoS₂ Nanosheets Shelled Micro-TiO₂ Hollow Spheres as Effective Multifunctional Electrocatalysts for HER, OER, and ORR. Nano Energy 2021, 82, No. 105750.
- (2) Kato, M.; Fujibayashi, N.; Abe, D.; Matsubara, N.; Yasuda, S.; Yagi, I. Impact of Heterometallic Cooperativity of Iron and Copper Active Sites on Electrocatalytic Oxygen Reduction Kinetics. ACS Catal. 2021, 11, 2356-2365.
- (3) Xiao, F.; Wang, Y.-C.; Wu, Z.-P.; Chen, G.; Yang, F.; Zhu, S.; Siddharth, K.; Kong, Z.; Lu, A.; Li, J.-C.; Zhong, C. J.; Zhou, Z.-Y.; Shao, M. Recent Advances in Electrocatalysts for Proton Exchange Membrane Fuel Cells and Alkaline Membrane Fuel Cells. Adv. Mater. 2021, 11, No. 2006292.
- (4) Zorko, M.; Martins, P. F. B. D.; Connell, J. G.; Lopes, P. P.; Markovic, N. M.; Stamenkovic, V. R.; Strmcnik, D. Improved Rate for the Oxygen Reduction Reaction in a Sulfuric Acid Electrolyte Using a Pt (111) Surface Modified with Melamine. ACS Appl. Mater. Interfaces 2021, 13, 3369-3376.
- (5) Zaman, S.; Huang, L.; Douka, A. I.; Yang, H.; You, B.; Xia, B. Y. Oxygen Reduction Electrocatalysts toward Practical Fuel Cells: Progress and Perspectives. Angew. Chem., Int. Ed. 2021, 133, 17976-17996.
- (6) Zhang, Q.; Kumar, P.; Zhu, X.; Daiyan, R.; Bedford, N. M.; Wu, K.-H.; Han, Z.; Zhang, T.; Amal, R.; Lu, X. Electronically Modified Atomic Sites Within a Multicomponent Co/Cu Composite for Efficient Oxygen Electroreduction. Adv. Energy Mater. 2021, 11, No. 2100303.
- (7) Wu, Z. P.; Shan, S.; Zang, S.-Q.; Zhong, C. J. Dynamic Core-Shell and Alloy Structures of Multimetallic Nanomaterials and Their Catalytic Synergies. Acc. Chem. Res. 2020, 53, 2913-2924.
- (8) Wu, Z. P.; Caracciolo, D. T.; Maswadeh, Y.; Wen, J.; Kong, Z.; Shan, S.; Vargas, J. A.; Yan, S.; Hopkins, E.; Park, K.; Sharma, A.; Ren, Y.; Petkov, V.; Wang, L.; Zhong, C. J. Alloying-Realloying Enabled High Durability for Pt-Pd-3d-Transition Metal Nanoparticle Fuel Cell Catalysts. Nat. Commun. 2021, 12, No. 859.
- (9) Li, S.; Liu, J.; Yin, Z.; Ren, P.; Lin, L.; Gong, Y.; Yang, C.; Zheng, X.; Cao, R.; Yao, S.; Deng, Y.; Liu, X.; Gu, L.; Zhou, W.; Zhu, J.; Wen, X.; Xu, B.; Ma, D. Impact of the Coordination Environment on Atomically Dispersed Pt Catalysts for Oxygen Reduction Reaction. ACS Catal. 2020, 10, 907-913.
- (10) Xu, H.; Shang, H.; Wang, C.; Du, Y. Recent Progress of Ultrathin 2D Pd-Based Nanomaterials for Fuel Cell Electrocatalysis. Small 2021, 17, No. 2005092.

- (11) Wu, J.; Shan, S.; Petkov, V.; Prasai, B.; Cronk, H.; Joseph, P.; Luo, J.; Zhong, C. J. Composition-Structure-Activity Relationships for Palladium-Alloyed Nanocatalysts in Oxygen Reduction Reaction: An Ex-situ/In-situ High Energy X-ray Diffraction Study. ACS Catal. **2015**, *5*, 5317–5327.
- (12) Wu, Z. P.; Shan, S.; Xie, Z.-H.; Kang, N.; Park, K.; Hopkins, E.; Yan, S.; Sharma, A.; Luo, J.; Wang, J.; Petkov, V.; Wang, L.; Zhong, C. J. Revealing the Role of Phase Structures of Bimetallic Nanocatalysts in Oxygen Reduction Reaction. ACS Catal. 2018, 8, 11302-11313.
- (13) Liu, Y.; Zhou, G.; Zhang, Z.; Lei, H.; Yao, Z.; Li, J.; Lin, J.; Cao, R. Significantly Improved Electrocatalytic Oxygen Reduction by an Asymmetrical Pacman Dinuclear Cobalt (II) Porphyrin-Porphyrin Dyad. Chem. Sci. 2020, 11, 87-96.
- (14) Qiao, M.; Wang, Y.; Mamat, X.; Chen, A.; Zou, G.; Li, L.; Hu, G.; Zhang, S.; Hu, X.; Voiry, D. Rational Design of Hierarchical, Porous, Co-Supported, N-Doped Carbon Architectures as Electrocatalyst for Oxygen Reduction. ChemSusChem 2020, 13, 741-748.
- (15) Zhang, H.; Zhao, M.; Liu, H.; Shi, S.; Wang, Z.; Zhang, B.; Song, L.; Shang, J.; Yang, Y.; Ma, C.; Zheng, L.; Han, Y.; Huang, W. Ultrastable FeCo Bifunctional Electrocatalyst on Se-Doped CNTs for Liquid and Flexible All-Solid-State Rechargeable Zn-Air Batteries. Nano Lett. 2021, 21, 2255-2264.
- (16) Khan, K.; Tareen, A. K.; Aslam, M.; Khan, S. A.; Khan, Q.; Khan, Q. U.; Saeed, M.; Saleemi, A. S.; Kiani, M.; Ouyang, Z.; Zhang, H.; Guo, Z. Fe-Doped Mayenite Electride Composite with 2D Reduced Graphene Oxide: as a Non-Platinum Based, Highly Durable Electrocatalyst for Oxygen Reduction Reaction. Sci. Rep. 2019, 9, No. 19809.
- (17) Chen, T.; Ma, J.; Chen, S.; Wei, Y.; Deng, C.; Chen, J.; Hu, J.; Ding, W. Construction of Heterostructured CoP/CN/Ni: Electron Redistribution Towards Effective Hydrogen Generation and Oxygen Reduction. Chem. Eng. J. 2021, 415, 129031-129040.
- (18) Wang, Y.; Carvalho, N. A.; Tan, S.; Gilbertson, L. M. Leveraging Electrochemistry to Uncover the Role of Nitrogen in the Biological Reactivity of Nitrogen-Doped Graphene. Environ. Sci.: Nano 2019, 6, 3525-3538.
- (19) Yang, K.; Zaffran, J.; Yang, B. Fast Prediction of Oxygen Reduction Reaction Activity on Carbon Nanotubes with a Localized Geometric Descriptor. Phys. Chem. Chem. Phys. 2020, 22, 890-895.
- (20) Ren, G.; Chen, S.; Zhang, J.; Zhang, N.; Jiao, C.; Qiu, H.; Liu, C.; Wang, H.-L. N-Doped Porous Carbon Spheres as Metal-Free Electrocatalyst for Oxygen Reduction Reaction. J. Mater. Chem. A **2021**, 9, 5751-5758.
- (21) Tao, H.; Liu, S.; Luo, J.-L.; Choi, P.; Liu, Q.; Xu, Z. Descriptor of Catalytic Activity of Metal Sulfides for Oxygen Reduction Reaction: A Potential Indicator for Mineral Flotation. J. Mater. Chem. A 2018, 6, 9650-9656.
- (22) Shi, C.; Ullah, S.; Li, K.; Wang, W.; Zhang, R.; Pan, L.; Zhang, X.; Zou, J.-J. Low-Temperature Synthesis of Ultrasmall Spinel Mn_xCo_{3-x}O₄ Nanoparticles for Efficient Oxygen Reduction. Chin. J. Catal. 2020, 41, 1818-1825.
- (23) Liang, Z.; Guo, H.; Zhou, G.; Guo, K.; Wang, B.; Lei, H.; Zhang, W.; Zheng, H.; Apfel, U.-P.; Cao, R. Metal-Organic-Framework-Supported Molecular Electrocatalysis for the Oxygen Reduction Reaction. Angew. Chem., Int. Ed. 2021, 60, 8553-8557.
- (24) Jiang, Y.; Xia, T.; Shen, L.; Ma, J.; Ma, H.; Sun, T.; Lv, F.; Zhu, N. Facet-Dependent Cu₂O Electrocatalysis for Wearable Enzyme-Free Smart Sensing. ACS Catal. 2021, 11, 2949-2955.
- (25) Saianand, G.; Gopalan, A.-I.; Lee, J.-C.; Sathish, C.; Gopalakrishnan, K.; Unni, G. E.; Shanbhag, D.; Dasireddy, V. D. B. C.; Yi, J.; Xi, S. B.; Al-Muhtaseb, A. H.; Vinu, A. Mixed Copper/ Copper-Oxide Anchored Mesoporous Fullerene Nanohybrids as Superior Electrocatalysts Toward Oxygen Reduction Reaction. Small 2020, 16, No. 1903937.
- (26) Xin, S.; Shen, J.; Liu, G.; Chen, Q.; Xiao, Z.; Zhang, G.; Xin, Y. Electricity Generation and Microbial Community of Single-Chamber Microbial Fuel Cells in Response to Cu₂O Nanoparticles/Reduced Graphene Oxide as Cathode Catalyst. Chem. Eng. J. 2020, 380, 122446-122455.

- (27) Kim, A.; Muthuchamy, N.; Yoon, C.; Joo, S. H.; Park, K. H. MOF-Derived Cu@Cu₂O Nanocatalyst for Oxygen Reduction Reaction and Cycloaddition Reaction. *Nanomaterials* **2018**, *8*, 138–151.
- (28) Li, Q.; Xu, P.; Zhang, B.; Tsai, H.; Zheng, S.; Wu, G.; Wang, H.-L. Structure-Dependent Electrocatalytic Properties of Cu₂O Nanocrystals for Oxygen Reduction Reaction. *J. Phys. Chem. C* **2013**, *117*, 13872–13878.
- (29) Li, J.; Zhou, N.; Song, J.; Fu, L.; Yan, J.; Tang, Y.; Wang, H. Cu-MOF-Derived Cu/Cu₂O Nanoparticles and CuN_xC_y Species to Boost Oxygen Reduction Activity of Ketjenblack Carbon in Al-Air Battery. ACS Sustainable Chem. Eng. **2018**, *6*, 413–421.
- (30) Gong, H.; Lu, S.; Strasser, P.; Yang, R. Highly Efficient AuNi-Cu₂O Electrocatalysts for the Oxygen Reduction and Evolution Reactions: Important Role of Interaction Between Au and Ni Engineered by Leaching of Cu₂O. *Electrochim. Acta* **2018**, 283, 1411–1417.
- (31) Wang, J.; Chen, F.; Jin, Y.; Johnston, R. L. Gold-Copper Aerogels with Intriguing Surface Electronic Modulation as Highly Active and Stable Electrocatalysts for Oxygen Reduction and Borohydride Oxidation. *ChemSusChem* **2018**, *11*, 1354–1364.
- (32) Wang, G.; Guan, J.; Xiao, L.; Huang, B.; Wu, N.; Lu, J.; Zhuang, L. Pd Skin on AuCu Intermetallic Nanoparticles: A Highly Active Electrocatalyst for Oxygen Reduction Reaction in Alkaline Media. *Nano Energy* **2016**, *29*, 268–274.
- (33) Zhang, N.; Chen, X.; Lu, Y.; An, L.; Li, X.; Xia, D.; Zhang, Z.; Li, J. Nano-Intermetallic AuCu₃ Catalyst for Oxygen Reduction Reaction: Performance and Mechanism. *Small* **2014**, *10*, 2662–2669.
- (34) Chiu, Y.-H.; Lindley, S. A.; Tsao, C.-W.; Kuo, M.-Y.; Cooper, J. K.; Hsu, Y.-J.; Zhang, J. Z. Hollow Au Nanosphere-Cu₂O Core-Shell Nanostructures with Controllable Core Surface Morphology. *J. Phys. Chem. C* **2020**, *124*, 11333–11339.
- (35) Kuo, M.-Y.; Hsiao, C.-F.; Chiu, Y.-H.; Lai, T.-H.; Fang, M.-J.; Wu, J.-Y.; Chen, J.-W.; Wu, C.-L.; Wei, K.-H.; Lin, H.-C.; Hsu, Y.-J. Au@Cu₂O Core@Shell Nanocrystals as Dual-Functional Catalysts for Sustainable Environmental Applications. *Appl. Catal., B* **2019**, 242, 499–506.
- (36) Li, J.-M.; Tsao, C.-W.; Fang, M.-J.; Chen, C.-C.; Liu, C.-W.; Hsu, Y.-J. TiO₂-Au-Cu₂O Photocathodes: Au-Mediated Z-Scheme Charge Transfer for Efficient Solar-Driven Photoelectrochemical Reduction. *ACS Appl. Nano Mater.* **2018**, *1*, 6843–6853.
- (37) Lin, Y.-K.; Chiang, Y.-J.; Hsu, Y.-J. Metal-Cu₂O Core-Shell Nanocrystals for Gas Sensing Applications: Effect of Metal Composition. *Sens. Actuators, B* **2014**, 204, 190–196.
- (38) Pu, Y.-C.; Lin, W.-H.; Hsu, Y.-J. Modulation of Charge Carrier Dynamics of $Na_xH_{2-x}Ti_3O_7$ -Au-Cu₂O Z-Scheme Nanoheterostructures Through Size Effect. *Appl. Catal., B* **2015**, *163*, 343–351.
- (39) Zhao, C.; Fu, H.; Yang, X.; Xiong, S.; Han, D.; An, X. Adsorption and Photocatalytic Performance of Au Nanoparticles Decorated Porous Cu₂O Nanospheres Under Simulated Solar Light Irradiation. *Appl. Surf. Sci.* **2021**, *545*, 149014–149028.
- (40) Chen, S.; Zhao, P.; Jiang, L.; Zhou, S.; Zheng, J.; Luo, X.; Huo, D.; Hou, C. Cu₂O-Mediated Assembly of Electrodeposition of Au Nanoparticles Onto 2D Metal-Organic Framework Nanosheets for Real-Time Monitoring of Hydrogen Peroxide Released from Living Cells. *Anal. Bioanal. Chem.* **2021**, *413*, 613–624.
- (41) Zhang, X.; Zhang, Y.; Huang, H.; Cai, J.; Ding, K.; Lin, S. Electrochemical Fabrication of Shape-Controlled Cu₂O with Spheres, Octahedrons and Truncated Octahedrons and Their Electrocatalysis for ORR. New J. Chem. 2018, 42, 458–464.
- (42) Lilloja, J.; Kibena-Põldsepp, E.; Sarapuu, A.; Douglin, J. C.; Käärik, M.; Kozlova, J.; Paiste, P.; Kikas, A.; Aruväli, J.; Leis, J.; Sammelselg, V.; Dekel, D. R.; Tammeveski, K. Transition-Metal- and Nitrogen-Doped Carbide-Derived Carbon/Carbon Nanotube Composites as Cathode Catalysts for Anion-Exchange Membrane Fuel Cells. ACS Catal. 2021, 11, 1920–1931.
- (43) Jiang, J.; Lim, Y.; Park, S.; Kim, S.-H.; Yoon, S.; Piao, L. Hollow Porous Cu Particles From Silica-Encapsulated Cu₂O Nanoparticle

- Aggregates Effectively Catalyze 4-Nitrophenol Reduction. *Nanoscale* **2017**, *9*, 3873–3880.
- (44) Chen, T.; Tian, L.; Chen, Y.; Liu, B.; Zhang, J. A Facile One-Pot Synthesis of Au/Cu₂O Nanocomposites for Nonenzymatic Detection of Hydrogen Peroxide. *Nanoscale Res. Lett.* **2015**, *10*, 252–259.
- (45) Xu, H.; Wang, W.; Zhou, L. A Growth Model of Single Crystalline Hollow Spheres: Oriented Attachment of Cu₂O Nanoparticles to the Single Crystalline Shell Wall. *Cryst. Growth Des.* **2008**, 8, 3486–3489.
- (46) Basu, M.; Sinha, A. K.; Pradhan, M.; Sarkar, S.; Govind; Pal, T. CuO Barrier Limited Corrosion of Solid Cu₂O Leading to Preferential Transport of Cu(I) Ion for Hollow Cu₇S₄ Cube Formation. *J. Phys. Chem. C* **2011**, *115*, 12275–12282.
- (47) Teo, J. J.; Chang, Y.; Zeng, H. C. Fabrications of Hollow Nanocubes of Cu₂O and Cu Via Reductive Self-Assembly of CuO Nanocrystals. *Langmuir* **2006**, 22, 7369–7377.
- (48) Wang, Y.; Lü, Y.; Zhan, W.; Xie, Z.; Kuang, Q.; Zheng, L. Synthesis of Porous Cu₂O/CuO Cages Using Cu-Based Metal-Organic Frameworks as Templates and Their Gas-Sensing Properties. *J. Mater. Chem. A* **2015**, *3*, 12796–12803.
- (49) Luo, J.; Liu, Y.; Niu, Y.; Jiang, Q.; Huang, R.; Zhang, B.; Su, D. Insight into the Chemical Adsorption Properties of CO Molecules Supported on Au or Cu and Hybridized Au-CuO Nanoparticles. *Nanoscale* **2017**, *9*, 15033–15043.
- (50) Klyushin, A. Y.; Greiner, M. T.; Huang, X.; Lunkenbein, T.; Li, X.; Timpe, O.; Friedrich, M.; Hävecker, M.; Knop-Gericke, A.; Schlögl, R. Is Nanostructuring Sufficient to Get Catalytically Active Au? *ACS Catal.* **2016**, *6*, 3372–3380.
- (51) Casaletto, M. P.; Longo, A.; Martorana, A.; Prestianni, A.; Venezia, A. M. XPS Study of Supported Gold Catalysts: The Role of ${\rm Au^0}$ and ${\rm Au^{+\delta}}$ Apecies as Active Sites. *Surf. Interface Anal.* **2006**, 38, 215–218.
- (52) Rui, N.; Zhang, F.; Sun, K.; Liu, Z.; Xu, W.; Stavitski, E.; Senanayake, S. D.; Rodriguez, J. A.; Liu, C.-J. Hydrogenation of CO_2 to Methanol on a $Au^{\delta+}$ -In₂O_{3-x} Catalyst. *ACS Catal.* **2020**, *10*, 11307—11317.
- (53) Li, X.; Zhang, J.; Liu, W.; Ren, Z.; Wang, H.; Zhu, Y.; Yang, Y.; Wei, M. Charge-Mediated Au $^{\delta_+}$ -Oxygen Vacancy Towards Glycerol Oxidation with Largely Improved Catalytic Performance. *Appl. Catal., A* **2020**, *598*, 117558–117567.
- (54) Xie, Y.; Wu, J.; Jing, G.; Zhang, H.; Zeng, S.; Tian, X.; Zou, X.; Wen, J.; Su, H.; Zhong, C.-J.; Cui, P. Structural Origin of High Catalytic Activity for Preferential CO Oxidation over CuO/CeO₂ Nanocatalysts with Different Shapes. *Appl. Catal., B* **2018**, 239, 665–676.
- (55) Chen, H.; Nishijima, M.; Wang, G.; Khene, S.; Zhu, M.; Deng, X.; Zhang, X.; Wen, W.; Luo, Y.; He, Q. The Ordered and Disordered Nano-Intermetallic AuCu/C Catalysts for the Oxygen Reduction Reaction: The Differences of the Electrochemical Performance. *J. Electrochem. Soc.* **2017**, *164*, F1654–F1661.
- (56) Xiao, H.; Li, B.; Zhao, M.; Li, Y.; Hu, T.; Jia, J.; Wu, H. Electrosynthesized ${\rm CuO_x/Graphene}$ by a Four-Electrode Electrolysis System for the Oxygen Reduction Reaction to Hydrogen Peroxide. *Chem. Commun.* **2021**, *57*, 4118–4121.
- (57) Hazarika, K. K.; Yamada, Y.; Matus, E. V.; Kerzhentsev, M.; Bharali, P. Enhancing the Electrocatalytic Activity Via Hybridization of Cu(I/II) Oxides with Co_3O_4 Towards Oxygen Electrode Reactions. *J. Power Sources* **2021**, 490, No. 229511.
- (58) Chhetri, K.; Dahal, B.; Mukhiya, T.; Tiwari, A. P.; Muthurasu, A.; Kim, T.; Kim, H.; Kim, H. Y. Integrated Hybrid of Graphitic Carbon-Encapsulated Cu_xO on Multilayered Mesoporous Carbon from Copper MOFs and Polyaniline for Asymmetric Supercapacitor and Oxygen Reduction Reactions. *Carbon* **2021**, *179*, 89–99.
- (59) Yu, X.; Zhao, C.; Zhang, T.; Liu, Z. Molecular and Dissociative O_2 Adsorption on the $Cu_2O(111)$ Surface. *Phys. Chem. Chem. Phys.* **2018**, 20, 20352–20362.